# Using VLF Transmitter Signals at LEO for Plasmasphere Model Validation

[1]M. E. Usanova, [2]R. A. Reid, [2]W. Xu, [2]R. A. Marshall, [3]M. J. Starks, [3]G. R. Wilson

[1]Laboratory for Atmospheric and Space Physics, University of Colorado, Boulder, Colorado, USA

[2]Ann & H.J. Smead Department of Aerospace Engineering Sciences, University of Colorado, Boulder, Colorado, USA

[3]Air Force Research Laboratory, Kirtland AFB, New Mexico, USA

## Abstract

This study presents analysis of very low frequency (VLF) transmitter signal measurements on the Very-Low-Frequency Propagation Mapper (VPM) CubeSat in low-Earth orbit. Six months of satellite operation provided good data coverage, used to build global statistical maps of VLF power distribution. The power distribution above four powerful transmitters is used as input for ray tracing to study signal propagation to the conjugate hemisphere in two plasmaspheric density models. The ray tracing results are further compared with VPM measurements to determine which model provides better agreement with observations. As ray propagation largely depends on the background plasma density distribution, this indirect method can be used for plasmaspheric density model validation as an alternative to multipoint in situ plasma measurements that may not be readily obtainable. In addition, it can be used to investigate Landau damping and ducted vs. non-ducted propagation of VLF signals.

**Plain language summary**

Very low frequency (VLF) transmitter signals at frequencies in the tens of kHz, used for military communication with submerged submarines, can be used to determine the plasma density distribution in near-Earth space. Here we demonstrate how a combination of VLF antenna measurements from low-Earth orbit and numerical modeling of VLF signal propagation can be applied to constrain plasma density profiles in the magnetosphere. This is an indirect method that can be used for plasmaspheric density model validation as an alternative to multipoint in situ plasma measurements that may not be readily obtainable.

**Main point #1.** At L<3, the diffusive equilibrium plasmasphere model provides much better agreement with observations than GCPM.

**Main point #2.** Signals from selected transmitters at L=1.17-2.87 propagate primarily in a non-ducted mode.

**Main point #3**. Landau damping is insignificant for the selected transmitters.

## 1. Introduction

Very low frequency (VLF) waves are natural and anthropogenic electromagnetic emissions in the 3-30 kHz frequency range. The major natural sources of these emissions are whistler-mode waves from lightning strikes (e.g., Helliwell, 2006 and references therein) and plasma instabilities in the magnetosphere (Burtis et al., 1969; Santolik et al., 2004). VLF waves reflect from below at the D region of the Earth's ionosphere (60-90 km altitude), and can propagate in the Earth-ionosphere waveguide nearly without attenuation (~2 dB/Mm) over long distances. They can also penetrate into seawater, which advanced their use for radio communication with submarines by deploying powerful VLF transmitter stations across the world. A fraction of VLF energy from ground-based sources leaks through the ionosphere and propagates through the magnetosphere as whistler-mode waves, where they can interact with energetic particles including radiation belt electrons.

VLF waves have important applications for remote sensing of the D region ionosphere, which responds dynamically to cosmic rays, solar and geomagnetic activity, lightning, earthquakes, solar eclipses, and more (Wait and Spies, 1964; Xu et al., 2019; Gross and Cohen, 2020). VLF wave propagation in the magnetosphere depends on the background plasma density. This property of VLF waves has long been used for diagnostics of the plasmasphere and cold plasma density reconstruction (Inan et al. 1977; Kimura et al., 2001; Lichtenberger et al., 2010; Ozhogin et al., 2012; Koronczay et al., 2018), and has led to the discovery of the outer boundary of the plasmasphere, the plasmapause (Gringauz, 1963; Carpenter, 1966).

VLF transmitters emit a significant amount of electromagnetic energy into the ionosphere and magnetosphere and modulate properties of the near-Earth plasma. Cohen and Inan (2012) constructed empirical models of the radiated power into the magnetosphere from L<2.6 transmitters using six years of data from the DEMETER mission. They found no detectable variation of signal intensity with geomagnetic conditions. However, they reported a significant power difference between daytime and nighttime observations, as expected. For nighttime intervals, they investigated transhemispheric signal attenuation and observed more than a factor of two average decrease in power. They attributed wave attenuation to Landau damping, either in the magnetosphere, or from scattered quasi-electrostatic waves emerging from the ionosphere. They also presented evidence of ionospheric heating. Němec and Parrot (2020) found that transmitter signals do not significantly change the mean plasma density and only slightly increase the electron temperature, though they can cause significant perturbations to both these quantities at distances up to ~200 km from the transmitter.

One of the important questions in relation to VLF transmitter signal propagation is whether the signals are ducted or non-ducted along plasma density gradients. Ducted waves propagate inside a density enhancement or depletion known as a duct, with wave energy and wave normals directed along the background magnetic field lines (Helliwell, 2006). Non-ducted waves propagate in a spatially smoothly varying medium, with wave normals being gradually refracted away from Earth (Cerisier, 1973). Clilverd et al. (2008) investigated the relative importance of the two types of propagation and found that the transition between ducted and non-ducted propagation occurs around L=1.5, being highly ducted at L>1.5 and mostly non-ducted below. This has been confirmed by more recent studies (e.g., Agapitov et al., 2014; Ma et al., 2017; Zhang et al., 2018). Even though there was a consensus about the demarcation between the ducted and non-ducted propagation regions, there is still ongoing discussion about VLF signal propagation throughout the inner magnetosphere and the relative contribution of ducted and non-ducted propagation modes. To answer this question, Gu et al. (2021) performed a statistical analysis of Van Allen Probes data at L=1.4-3.4 and showed that non-ducted propagation dominates over ducted propagation in both the occurrence and intensity of transmitter signals (only a third of the observed wave energy density was ducted). Using ray tracing, they also concluded that the latitudinal distribution of wavevectors corresponded to non-ducted propagation.

Another important property of VLF waves is their potential to resonantly interact with radiation belt electrons, causing electron loss into the atmosphere (Gamble et al., 2008; Foster et al., 2016). This process takes place predominantly over the range 1.3 ≤ L ≤ 2.4 (Abel and Thorne, 1998). Its efficacy depends on the wave being ducted or non-ducted. While both types of waves can cause electron precipitation, ducted VLF waves are much more effective in driving radiation belt pitch angle scattering (Rodger et al., 2010). Non-ducted waves interact with electrons through Landau resonance, as well as cyclotron resonances at higher equatorial pitch angles (Abel and Thorne, 1998; Ross et al., 2019). Thus, knowledge of VLF signal propagation is not only important for communication applications but also for understanding of the outer radiation belt dynamics (Albert et al., 2020 and references therein).

In this paper, we apply a combination of transmitter signal observations at LEO and ray tracing to provide validation of plasmaspheric density models. We also examine ducted vs. non-ducted propagation using four VLF transmitters located at different L-shells, from L=1.17 to L=2.87. In Section 2, we describe instrumentation used for this study. In Section 3, we discuss VLF transmitter signal analysis. In Section 4, we present full wave simulations used to constrain wave properties above the transmitter location. In Section 5, we introduce VLF signal ray tracing, and Section 6 summarizes our study.

## 2. Instrumentation

The Very-Low-Frequency Propagation Mapper (VPM) is an Air Force Research Laboratory (AFRL) CubeSat designed to study very low frequency (VLF) wave propagation from low-Earth orbit (LEO). The science goals of the VPM mission are to measure VLF signals broadcasted by the AFRL Demonstration and Science Experiments (DSX) mission (Scherbarth et al., 2009), and to study natural and anthropogenic signals from 300 Hz to 40 kHz in the near-Earth space environment. The VPM CubeSat was deployed into a 500 km orbit with 51.6° inclination in February 2020 and collected single electric field dipole antenna data for six months before communication with the spacecraft was lost (Marshall et al., 2021). For this study, we used VPM survey data recorded at a 26 s cadence and a 78 Hz frequency resolution.

## 3. Observations

An example of a VPM electric field spectrogram from March 12, 2020 is shown in Figure 1. VLF transmitter signals are narrow-band emissions at ~10-30 kHz, which appear to be transient in the spectra as the spacecraft flies over each transmitter. As the satellite orbited Earth, it passed through the daytime and nighttime ionosphere characterized by varying electron density that affects the VLF signal structure. During daytime, excess spacecraft noise is evident in the spectra due to battery charging circuitry. The broad-band signal typical of daytime or sunlit conditions was removed from further analysis, so only nighttime data were included in our statistics.

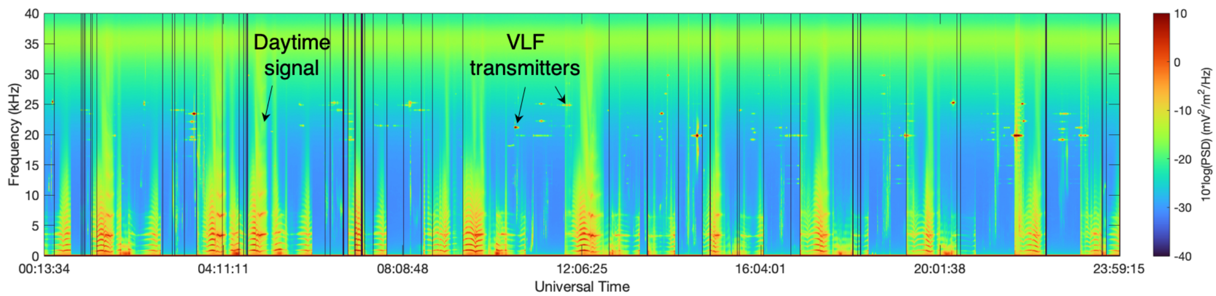


**Figure 1.** Electric field spectrogram from March 12, 2020. The discrete narrow band emissions correspond to VLF transmitters. The broad-band signal is typical of daytime sunlit conditions.

For our statistical analysis that spans the entire mission duration, we selected four powerful transmitters: three (NPM, 21.4 kHz; NLK, 24.8 kHz; NAA, 24.0 kHz) in the northern and one (NWC, 19.8 kHz) in the southern hemisphere, as listed in Table 1.

| Name/ Call sign | Location | GEO lon,° | GEO lat,° | Conjugate GEO lon,° | Conjugate GEO lat,° | L-shell | Declination,° | Frequency (kHz) |
|---|---|---|---|---|---|---|---|---|
| NPM | Lualualei, Hawaii, USA | -158.15 | 21.42 | -165.93 | -19.43 | 1.17 | 9.52 | 21.4 |
| NLK | Jim Creek, Washington USA | -121.91 | 48.20 | -152.2 | -54.81 | 2.87 | 15.53 | 24.8 |
| NAA | Cutler, Maine, USA | -67.29 | 44.65 | -57.06 | -65.20 | 2.68 | -16.03 | 24.0 |
| NWC | Exmouth, Western Australia | 114.17 | -21.82 | 112.78 | 37.14 | 1.41 | 0.23 | 19.8 |

**Table 1.** Transmitter parameters. L-shell and declination are at a 100 km altitude above the transmitter. Conjugate location is calculated at a 500 km altitude using the CGM

model, https://omniweb.gsfc.nasa.gov/vitmo/cgm.html. Transmitter's locations (red stars) and conjugate points (blue stars) are shown in Figures 2,6,7.

Within a 20-degree radius around each transmitter, VPM collected between ~2000 and 3000 data points or, precisely, 14.7, 16.0, 14.6, 22.7 hours of measurements around NPM, NLK, NAA, and NWC, respectively. For frequencies corresponding to the selected transmitters, we binned data on a 2x2 degree grid and calculated average electric field power spectral density in each bin. For each transmitter, the conjugate location is determined by the magnetic field declination, tilted westward for NPM, NLK and eastward for NAA. The declination at NWC is minimal so that the conjugate location is almost directly north of the NWC transmitter. Figure 2 shows that the signal intensity is maximum above the transmitter and deviates from the magnetically conjugate location in the opposite hemisphere, indicative of the transmitter signal not travelling along the background magnetic field lines. The measured power distributions in the conjugate region are consistent with non-ducted propagation, as predicted in our ray-tracing simulations (discussed in Section 5 below).

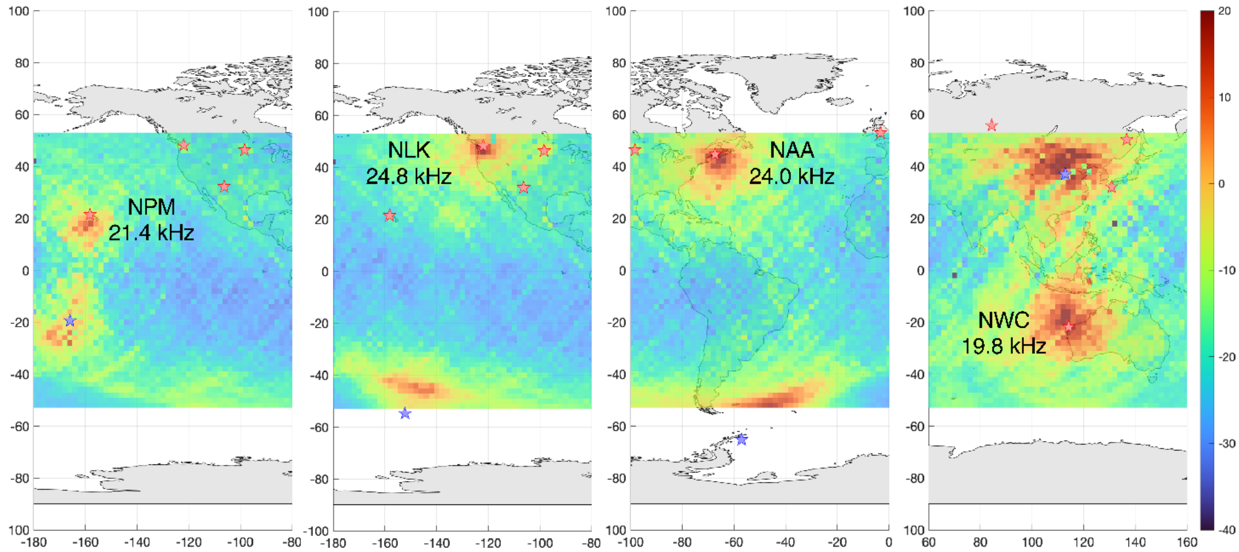


**Figure 2.** Average electric field power spectral density along the satellite tracks in the vicinity of the NPM (21.4 kHz), NLK (24.8 kHz), NAA (24.0 kHz) and NWC (19.8 kHz) transmitters and their conjugate locations. The red and the blue stars show the VLF transmitter positions and their conjugate locations, respectively. Data binned at 2x2 degrees. Colorbar units correspond to 10*log(PSD) in $(mV/m)^2/Hz$.

## 4. Full wave simulations

Full wave simulations (Lehtinen and Inan, 2008; 2009) are used to justify parallel wave propagation above transmitters, further used as boundary conditions in ray tracing. Figure 3 shows the wave propagation pattern around the NWC transmitter under the median ionospheric electron density condition. This electron density profile is specifically taken from the Faraday International Reference Ionosphere (FIRI) model (Friedrich et al., 2018), and corresponds to the 50th percentile of nighttime conditions. Here, the +x direction is north, -x is south, +y is west, and -y is east. NWC is in the southern hemisphere, so that the magnetic field (and k-vectors) tilt from vertical towards the north

(+x). Panel a) shows the electric field amplitude in the horizontal plane at the 500 km altitude above NWC. The result is reasonably symmetric east-west as the NWC transmitter declination is only 0.3 degrees. Panel b) shows the wave normal angle (WNA; the angle between the k-vector and the local magnetic field line) in the horizontal plane. In the north direction, the wave normals are close to zero, so it is easier to follow the background magnetic field. For rays that start southward below the ionosphere, there is a stronger angular rotation towards the magnetic field direction, and so they may not quite reach parallel propagation. Panel c) shows the x-z variation in amplitude and the north-south tilt of the wave patterns. The k-vectors below the ionosphere are radial away from the transmitter. Once the rays reach the D-region, k-vectors rotate into the magnetic field direction. Overall, these results show that the initial wave normal angle at 500 km altitude is within ~20 degrees of parallel to the background magnetic field. Similar full-wave simulations have been conducted for the other VLF transmitters of interest, and the results give comparable wave normal angle distributions.

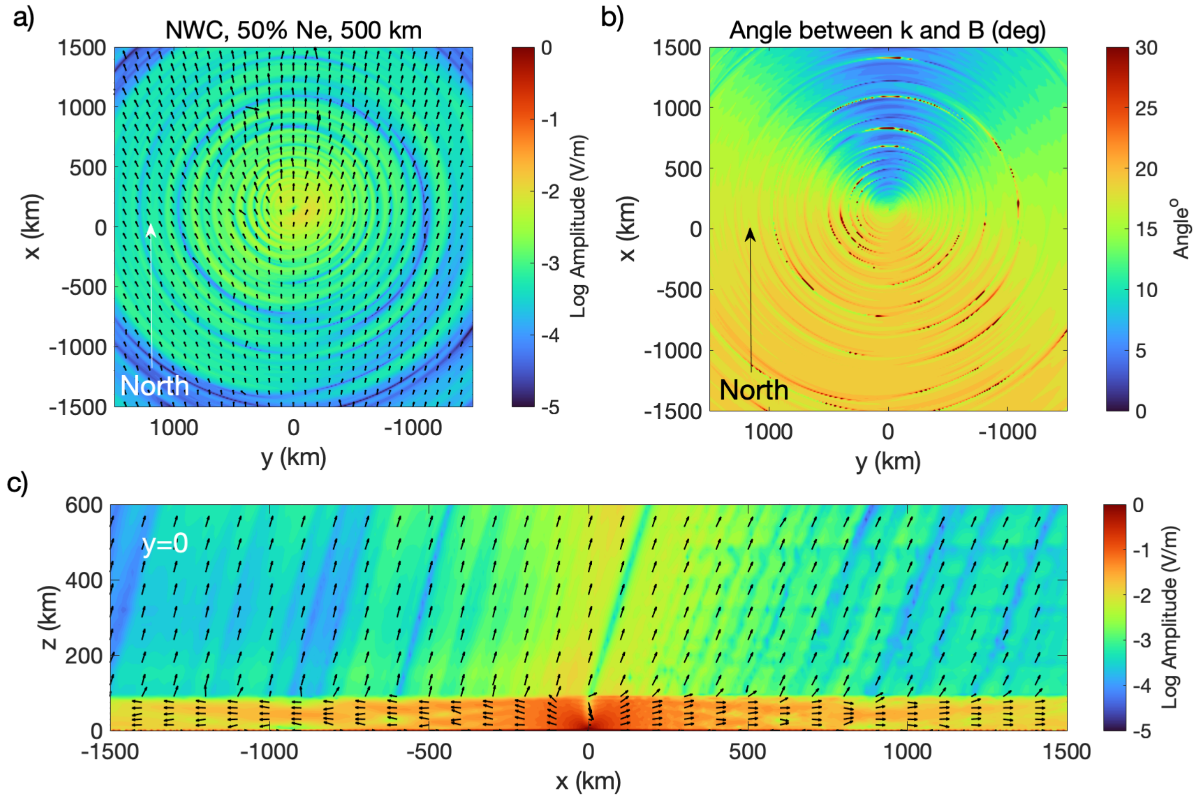


**Figure 3.** Wave propagation pattern from full wave simulations. x is the north-south direction; positive x corresponds to north in all three panels. y is in the east-west direction; positive y is westward. a) electric field amplitude in the horizontal plane at the 500 km altitude above NWC; b) wave normal angle in the horizontal plane at 500 km; c) electric field amplitude as a function of altitude and distance from NWC in the north-south direction.

## 5. Ray tracing

The Stanford VLF ray tracing program was used to compute 3D ray paths (Reid et al., submitted). The code was originally developed by Inan and Bell (1977); it has since been updated and used in many studies (e.g., Bell et al., 2002; Botnik et al., 2007). The ray tracer utilizes an adaptive time stepping scheme to propagate ray paths. Rays were initialized at 500 km above the transmitter with field-aligned wave normal angles to simplify the process. Simulations conducted with the initial WNA +/- 10 or 20 degrees (not shown here) did not have a major impact on the ray propagation or the ray final location in the conjugate region. Rays were then propagated until the altitude below 500 km (closer to 475 km) was reached in the conjugate hemisphere, or if the ray met one of the specified exit conditions in the ray tracer (error exceeded tolerance, maximum simulation time exceeded or maximum time steps exceeded). Simulation conditions were set to ensure the majority of rays in each simulation were propagated until the specified altitude was reached in the conjugate hemisphere. We assumed a changing Earth's background magnetic field and electron density along ray paths and used the International Geomagnetic Reference Field (IGRF) 13th Generation magnetic field model (Alken et al., 2021) and two different plasmaspheric density models.

As plasma density is crucial for ray propagation and strongly affects ray refraction and damping, we used our results to validate a diffusive equilibrium (DE) analytical model described by Angerami and Thomas (1964) and the global core plasma model (GCPM) developed by Gallagher et al. (2000). The DE model is used with the following parameters. The geocentric distance to the base of the diffusive equilibrium model is set to 400 km, the temperature and reference electron density at the base of the diffusive equilibrium model are 1000 K and $2^{11}$ $m^{-3}$, respectively; $H^+$ and $O^+$ concentrations are 50%.

GCPM provides empirically derived core plasma density and ion composition ($H^+$, $He^+$, and $O^+$) as a function of geomagnetic and solar conditions throughout the inner magnetosphere. The model is based on data from DE/RIMS, DE/PWI, and ISEE/PWI and merges with the International Reference Ionosphere (IRI; Bilitza, 2001) at low altitudes. It is composed of separate models for the plasmasphere, plasmapause, trough, and polar cap. We used a simplified version of the GCPM model described by Sousa (2018); however, inside L=4 this model is nearly identical to the original GCPM model.

Plasma density profiles for the DE and GCPM models are shown in Figure 4. The profiles are plotted for quiet geomagnetic conditions, Kp=1 being the average value during the period of VPM operation. The DE model peaks in density at an altitude of 325 km and has the plasmapause at L~5.2. The density in the GCPM model sharply drops from the inner boundary at ~70 km to 1590 km and then gradually decreases without the well-defined plasmapause, typical for geomagnetic quiescence. Ozhogin et al. (2014) evaluated electron density profiles of five diffusive equilibrium models against IMAGE RPI measurements between L=1.5 and 4.5 (see their Figure 1, also plotted over Figure 4 here). The IMAGE RPI densities are shown by the black line and dots. Other curves correspond to five different DE models evaluated in Ozhogin et al. (2014). The DE model used in our study matches the IMAGE RPI density profiles at L=2-3 and slightly overestimates electron density at L=1.5-2. The GCPM model underestimates density in the whole L-shell range covered by RPI. Other than gradients present in these models, no plasma irregularities or ducts are included in simulations.

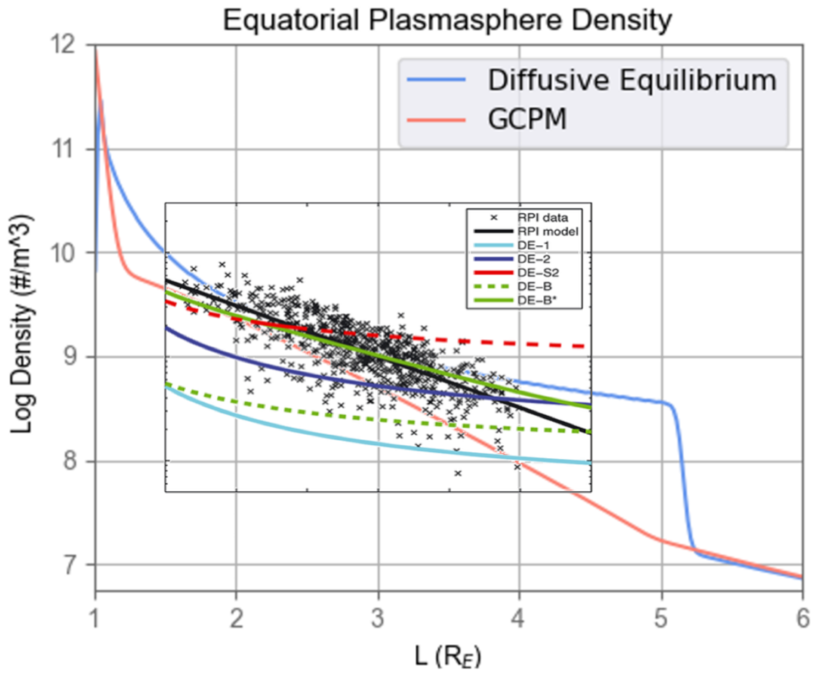


**Figure 4.** Plasmaspheric density profiles for diffusive equilibrium (orange) and GCPM (blue) calculated for Kp=1. Overlaid, is Figure 1 from Ozhogin et al. (2014). The IMAGE RPI densities are shown by the black line and dots. The curves correspond to five different DE models evaluated in Ozhogin et al. (2014).

We also investigated the effect of Landau damping on wave attenuation and growth and computed it along the ray path as described by Brinca (1972). Landau damping depends on the propagation medium, and as the medium properties change spatially, the damping factor is computed at every step. The final normalized damping factor was applied to each ray that reached the specified minimum altitude in the conjugate hemisphere to scale the wave power implemented in the Stanford ray tracer as described by Bortnik (2004). We found that Landau damping was negligible at the VLF transmitter frequencies and did not affect signal amplitude at the conjugate location (for both plasmaspheric models), hence we do not show the ray tracing results including Landau damping here. Top and bottom panels in Figure 5 show plasma density and along ray paths and ray wave normal angle, respectively, traced from the location above the NWC transmitter to the conjugate hemisphere in the DE and GCPM density models. The rays begin with wave normal angles parallel to the background magnetic field above the transmitter, begin to deviate to 10-20 degrees, and then shift back towards zero again. They then deviate towards 90 degrees once they are in the opposite hemisphere. This pattern shows that rays reach the second WNA=0 point at a location that trends with source latitude.

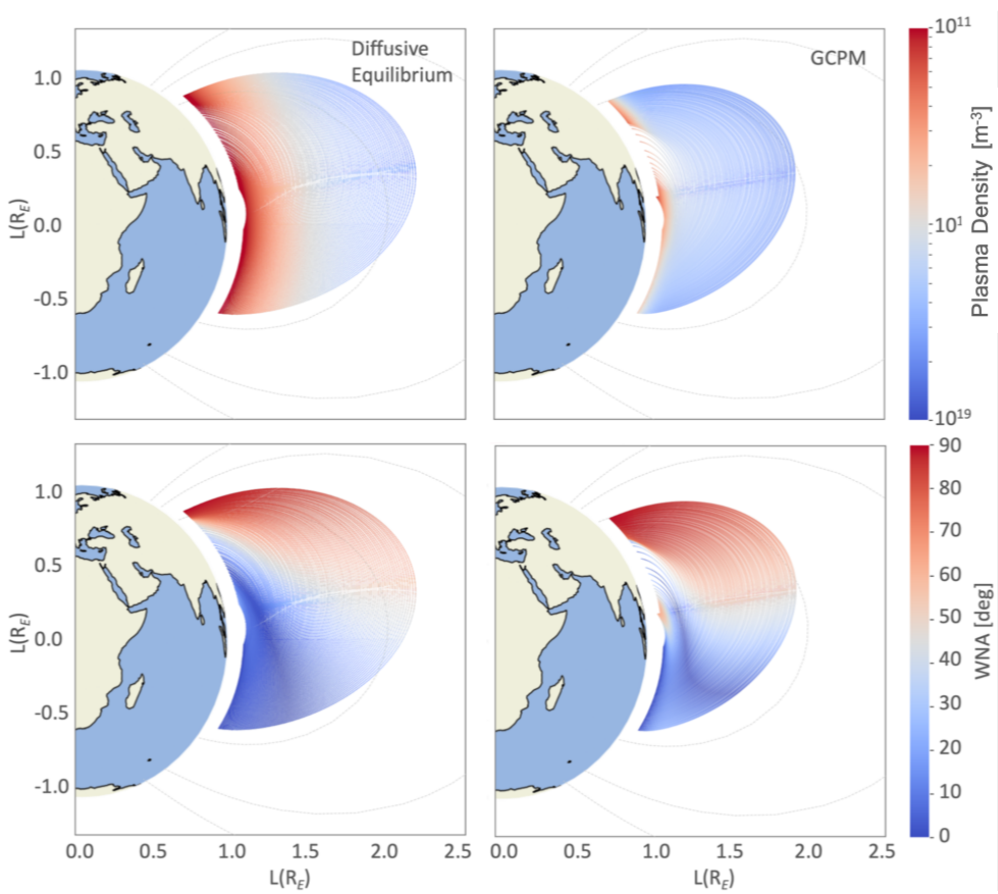


**Figure 5.** Plasma density (top row) and WNA (bottom row) in the diffusive equilibrium (left column) and GCPM (right column) models.

Figure 6 shows raytracing results for the diffusive equilibrium model. The initial ray power distribution over the transmitter was obtained from averaged VPM measurements by smoothing and interpolating onto a finer, 0.1x0.1-degree grid using linear regression. The power distribution in the conjugate hemisphere was renormalized by the ray density to account for their latitudinal spread during propagation.

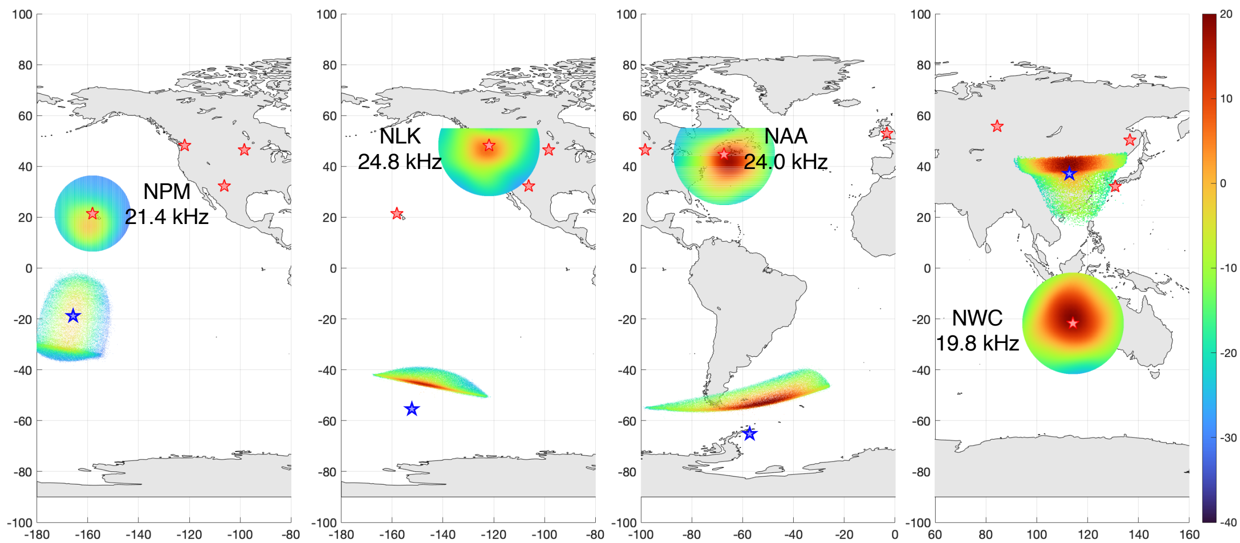


**Figure 6.** Average electric field power spectral density in a ray tracing output from the diffusive equilibrium model. The NPM (21.4 kHz), NLK (24.8 kHz), NAA (24.0 kHz) and NWC (19.8 kHz) transmitters and their conjugate locations are shown by the red and the blue stars, respectively. Colorbar units correspond to 10*log(PSD) in $(mV/m)^2$/Hz.

Likewise, Figure 7 shows raytracing results for the GCPM model. Both sets of runs (DE and GCPM) reproduce the dipole tilt as they sample the same magnetic field model. The differences arise from plasmaspheric density profiles which ray propagation paths are extremely sensitive to. As compared to VPM measurements, DE provides good agreement with observations. GCPM results in a ray latitudinal spread and power distribution patterns not seen in data.

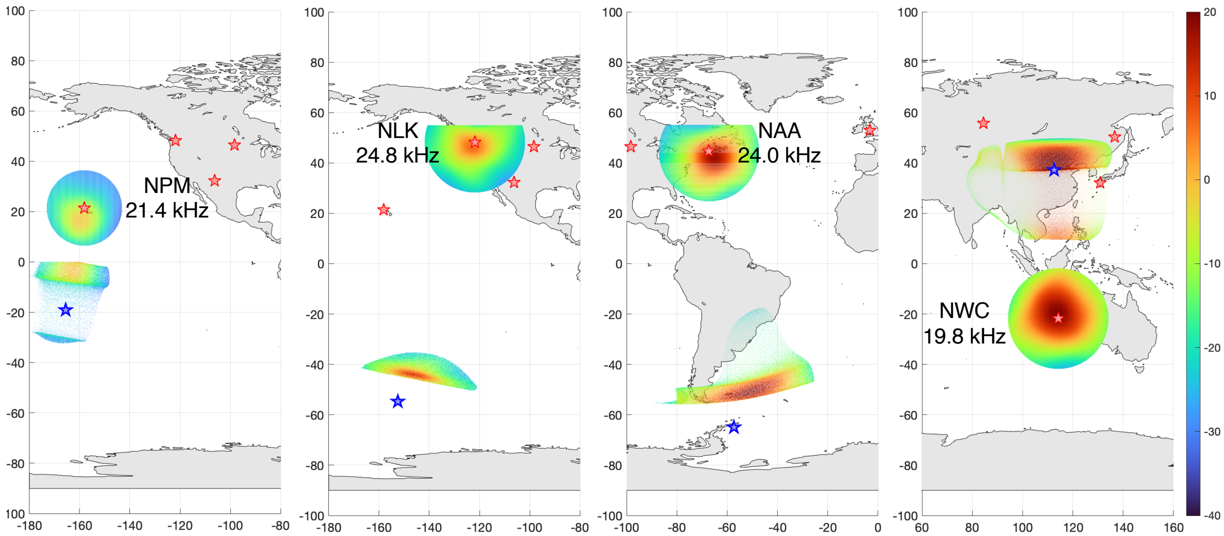


**Figure 7.** Average electric field power spectral density in a ray tracing output from the GCPM model. The NPM (21.4 kHz), NLK (24.8 kHz), NAA (24.0 kHz) and NWC (19.8 kHz) transmitters and their conjugate locations are shown by the red and the blue stars, respectively. Colorbar units correspond to 10*log(PSD) in $(mV/m)^2/Hz$.

Both models do not include density ducts and simulate non-ducted propagation for all four transmitters, the simulation results being consistent with observations of wave power at LEO. However, these results do not support earlier conclusions that VLF transmitter propagation is mostly ducted at L>1.5. They are more in line with the recent study by Gu et al., 2021 showing that transmitter signals are largely non-ducted in a wide range of L-shells from L=1.4 to 3.4.

## 6. Summary and conclusions

Several months of VPM satellite operation provided good data coverage and an opportunity to study VLF transmitter signal propagation statistically. As plasma density alters VLF wave propagation causing refraction and attenuation, observations were combined with ray tracing in order to compare and validate plasmaspheric density models. In addition, a full wave model was employed to simulate wave normal angles above transmitters and to constrain boundary conditions for ray tracing. For our comparative analysis, we tested the DE model implemented in the Stanford ray tracer and GCPM. We concluded that at L<3, the DE model provides much better agreement with observations. We could not investigate the performance of these models at higher L-shells due to the VPM orbit inclination. We also found that the electric power distribution from selected transmitters at L=1.17-2.87 is consistent with simulated non-ducted propagation. These results are different from those previously reported that lower-L (L<1.5) transmitter signals propagate as non-ducted, while at L>1.5 the signals become mostly ducted. In relation to Cohen and Inan (2012), we conclude that VLF signals at ~20 kHz frequencies do not experience noticeable Landau damping over one inter-hemispheric pass. Overall, the technique described here can be used for validation of other plasmaspheric models and will be further developed to study ducted and non-ducted propagation of VLF signals in the inner magnetosphere.

## Acknowledgements

VPM data processing and analysis was conducted under contract AFRL FA9453-19-C-0400 to Atmospheric and Environmental Research (AER), Incorporated and subcontract

P2247-04 to the University of Colorado Boulder. MEU is thankful for support from the International Space Sciences Institute (ISSI) international teams program.

## Data availability

The data that support the findings of this study are available from AFRL. Restrictions apply to the availability of these data; data and simulation output are available from the authors with the permission of AFRL.

## References:

Abel, B., & Thorne, R. M. (1998). Electron scattering loss in earth's inner magnetosphere: 2. Sensitivity to model parameters. *Journal of Geophysical Research*, 103(A2), 2397–2407. https://doi.org/10.1029/97JA02920.

Agapitov, O. V., Artemyev, A. V., Mourenas, D., Kasahara, Y., & Krasnoselskikh, V. (2014). Inner belt and slot region electron lifetimes and energization rates based on akebono statistics of whistler waves. *Journal of Geophysical Research: Space Physics*, 119(4), 2876–2893. https://doi.org/10.1002/2014JA019886.

Albert, J. M., Starks, M. J., Selesnick, R. S., Ling, A. G., O'Malley, S., & Quinn, R. A. (2020). VLF transmitters and lightning-generated whistlers: 2. Diffusion of radiation belt electrons. *Journal of Geophysical Research: Space Physics*, 125, e2019JA027030. https://doi.org/10.1029/2019JA027030.

Alken, P., Thébault, E., Beggan, C.D. et al. International Geomagnetic Reference Field: the thirteenth generation. *Earth Planets Space 73,* 49 (2021). https://doi.org/10.1186/s40623-020-01288-x.

Angerami, J. J., and Thomas, J. O. (1964), Studies of planetary atmospheres: 1. The distribution of electrons and ions in the Earth's exosphere, *J. Geophys. Res.*, 69( 21), 4537– 4560, doi:10.1029/JZ069i021p04537.

Bilitza, D. (2001), International Reference Ionosphere 2000, *Radio Sci.*, 36( 2), 261– 275, doi:10.1029/2000RS002432.

Bortnik, J. (2004). Precipitation of radiation belt electrons by lightning-generated magnetospherically reflecting whistler waves. Stanford University.

Bortnik, J., Thorne, R. M., Meredith, N. P., and Santolik, O. (2007), Ray tracing of penetrating chorus and its implications for the radiation belts, *Geophys. Res. Lett.*, 34, L15109, doi:10.1029/2007GL030040.

Brinca, A. L. (1972), On the stability of obliquely propagating whistlers, *J. Geophys. Res.*, 77( 19), 3495– 3507, doi:10.1029/JA077i019p03495.

Burtis, W. J., and Helliwell, R. A. (1969), Banded chorus—A new type of VLF radiation observed in the magnetosphere by OGO 1 and OGO 3, *J. Geophys. Res.*, 74(11), 3002–3010, doi:10.1029/JA074i011p03002.

Carpenter, D. L. (1966), Whistler studies of the plasmapause in the magnetosphere: 1. Temporal variations in the position of the knee and some evidence on plasma motions near the knee, *J. Geophys. Res.*, 71( 3), 693– 709, doi:10.1029/JZ071i003p00693.

Cerisier, J. (1973). A theoretical and experimental study of non-ducted VLF waves after propagation through the magnetosphere. *Journal of Atmospheric and Terrestrial Physics*, 35(1), 77–94. https://doi.org/10.1016/0021-9169(73)90217-1.

Clilverd, M. A., Rodger, C. J., Gamble, R., Meredith, N. P., Parrot, M., Berthelier, J. J., & Thomson, N. R. (2008). Ground-based transmitter signals observed from space: Ducted or nonducted? *Journal of Geophysical Research*, 113, A04211. https://doi.org/10.1029/2007JA012602

Cohen, M. B., and Inan, U. S. (2012), Terrestrial VLF transmitter injection into the magnetosphere, *J. Geophys. Res.*, 117, A08310, doi:10.1029/2012JA017992.

Foster, J. C., Erickson, P. J., Baker, D. N., Jaynes, A. N., Mishin, E. V., Fennel, J. F., Li, X., Henderson, M. G., and Kanekal, S. G. (2016), Observations of the impenetrable barrier, the plasmapause, and the VLF bubble during the 17 March 2015 storm, *J. Geophys. Res. Space Physics*, 121, 5537– 5548, doi:10.1002/2016JA022509.

Friedrich, M., C. Pock, and K. Torkar (2018), FIRI-2018, an updated empirical model of the lower ionosphere, J. Geophys. Res. Space Physics, 123(8), 6737–6751.

Gallagher, D. L., Craven, P. D., and Comfort, R. H. (2000), Global core plasma model, *J. Geophys. Res.*, 105( A8), 18819– 18833, doi:10.1029/1999JA000241.

Gamble, R. J., C. J. Rodger, M. A. Clilverd, J.-A. Sauvaud, N. R. Thomson, S. L. Stewart, R. J. McCormick, M. Parrot, and J.-J. Berthelier (2008), Radiation belt electron precipitation by man-made VLF transmissions, *J. Geophys. Res., 113*, A10211, doi:10.1029/2008JA013369.

Gringauz, K. I. (1963), The structure of the ionized gas envelope of earth from direct measurements in the USSR of local charged particle concentrations, *Planet. Space Sci., 11(3)*, 281–296, doi: 10.1016/0032-0633(63)90030-8.

Gross, N. C., & Cohen, M. B. (2020). VLF remote sensing of the *D* region ionosphere using neural networks. *Journal of Geophysical Research: Space Physics*, 125, e2019JA027135. https://doi.org/10.1029/2019JA027135.

Gu, W., Chen, L., Xia, Z., & Horne, R. B. (2021). Direct evidence reveals transmitter signal propagation in the magnetosphere. *Geophysical Research Letters*, 48, e2021GL093987. https://doi.org/10.1029/2021GL093987.

Helliwell, R.A. (2006). Whistlers and Related Ionospheric Phenomena. Dover Publications, Inc. ISBN 978-0-486-44572-4. Originally published by Stanford University Press, Stanford, California (1965).

Inan, U. S., and Bell, T. F. (1977), The plasmapause as a VLF wave guide, *J. Geophys. Res.*, 82( 19), 2819– 2827, doi:10.1029/JA082i019p02819.

Lehtinen, N. G., and U. S. Inan (2008), Radiation of ELF/VLF waves by harmonically varying currents into a stratified ionosphere with application to radiation by a modulated electrojet, *J. Geophys. Res. Space Physics,* 113*,* A06301, doi:10.1029/2007JA012911.

Lehtinen, N. G., and U. S. Inan (2009), Full-wave modeling of transionospheric propagation of VLF waves, *Geophys. Res. Lett.,* 36*,* L03104, doi:10.1029/2008GL036535.

Lichtenberger, J., Ferencz, C., Hamar, D., Steinbach, P., Rodger, C. J., Clilverd, M. A., & Collier, A. B. (2010). Automatic whistler detector and analyzer system: Implementation of the analyzer algorithm. *Journal of Geophysical Research*, 115, A12214. https://doi.org/10.1029/2010JA015931.

Kimura, I., Kasahara, Y., & Oya, H. (2001). Determination of global plasmaspheric electron density profile by tomographic approach using omega signals and ray tracing. *Journal of Atmospheric and Solar-Terrestrial Physics*, 63, 1157–1170. https://doi.org/10.1016/S1364-6826(00)00220-0.

Koronczay, D., Lichtenberger, J., Juhász, L., Steinbach, P., & Hospodarsky, G. B. (2018). VLF transmitters as tools for monitoring the plasmasphere. *Journal of Geophysical Research: Space Physics*, 123, 9312– 9324. https://doi.org/10.1029/2018JA025802.

Ma, Q., Mourenas, D., Li, W., Artemyev, A., & Thorne, R. M. (2017). VLF waves from ground-based transmitters observed by the Van Allen Probes: Statistical model and effects on plasmaspheric electrons. *Geophysical Research Letters*, 44(13), 6483–6491. https://doi.org/10.1002/2017GL073885.

Marshall, R. A., Sousa, A., Riley, R., Wilson, G., Starks, M., et al. (2021), The Micro-Broadband Receiver (µBBR) on the Very-Low-Frequency Propagation Mapper CubeSat, Journal of Geophysical Research: Earth and Space Science, 8 (11), https://doi.org/10.1029/2021EA001951.

Němec, F., Pekař, J., & Parrot, M. (2020). NWC transmitter effects on the nightside upper ionosphere observed by a low-altitude satellite. *Journal of Geophysical Research: Space Physics*, 125, e2020JA028660. https://doi.org/10.1029/2020JA028660.

Ozhogin, P., Tu, J., Song, P., & Reinisch, B. W. (2012). Field-aligned distribution of the plasmaspheric electron density: An empirical model derived from the IMAGE RPI measurements. *Journal of Geophysical Research*, 117, A06225. https://doi.org/10.1029/2011JA017330.

Ozhogin, P., Song, P., Tu, J., and Reinisch, B. W. (2014), Evaluating the diffusive equilibrium models: Comparison with the IMAGE RPI field-aligned electron density measurements, *J. Geophys. Res. Space Physics*, 119, 4400– 4411, doi:10.1002/2014JA019982.

Reid, R.A., R. A. Marshall, M. J. Starks, M. E. Usanova, G. R. Wilson, W. R. Johnston, J. C. Sanchez, Y.-J. Su, G. P. Ginet, P. Song, I. A. Galkin, Active VLF transmission experiments between the DSX and VPM spacecraft (submitted to JGR Space Phys.)

Rodger, C. J., Carson, B. R., Cummer, S. A., Gamble, R. J., Clilverd, M. A., Green, J. C., Sauvaud, J.-A., Parrot, M., and Berthelier, J.-J. (2010), Contrasting the efficiency of radiation belt losses caused by ducted and nonducted whistler-mode waves from ground-based transmitters, *J. Geophys. Res.*, 115, A12208, doi:10.1029/2010JA015880.

Ross, J. P. J., Meredith, N. P., Glauert, S. A., Horne, R. B., & Clilverd, M. A.(2019). Effects of VLF transmitter waves on the inner belt and slot region. *Journal of Geophysical Research: Space Physics*, 124(7), 5260–5277. https://doi.org/10.1029/2019JA026716.

Santolik, O., D. A. Gurnett, and J. S. Pickett (2004), Multipoint investigation of the source region of storm-time chorus, *Ann. Geophys.*, 22, 2555–2563.

Scherbarth, M., Smith, D., Adler, A., Stuart, J., & Ginet, G. (2009). AFRL's demonstration and science experiments (DSX) mission. In *Solar physics and space weather instrumentation III* (Vol. 7438, p. 74380B). https://doi.org/10.1117/12.824898.

Sousa, A. P. (2018). Global and seasonal effects of lightning-induced electron precipitation. Stanford University.

Wait, J. R., & Spies, K. P. (1964). Characteristics of the Earth-ionosphere waveguide for VLF radio waves (Tech. Rep.). Boulder, CO: National Bureau of Standards.

Xu, W., R. A. Marshall, A. Kero, E. Turunen, D. Drob, J. Sojka, and D. Rice (2019), VLF measurements and modeling of the D-region response to the 2017 total solar eclipse, IEEE Transactions on Geoscience and Remote Sensing, 57(10), 7613–7622.

Zhang, Z., Chen, L., Li, X., Xia, Z., Heelis, R. A., & Horne, R. B. (2018). Observed propagation route of VLF transmitter signals in the magnetosphere. Journal of Geophysical Research: Space Physics, 123(7), 5528–5537. https://doi.org/10.1029/2018JA025637.